

## Impact of Embedding Cavity Design on Thermal History between Layers in Polymer Material Extrusion Additive Manufacturing

Swapnil Sinha<sup>1</sup> and Nicholas A. Meisel<sup>2</sup>

<sup>1</sup>Department of Mechanical Engineering, Penn State, University Park, PA 16802

<sup>2</sup>School of Engineering Design, Technology, and Professional Programs, Penn State, University Park, PA 16802

### Abstract

By pausing an additive manufacturing process in mid-print, it is possible to create multifunctional structures through strategic insertion of foreign components. However, in polymer material extrusion, previous research has shown that pausing the build decreases the eventual strength of the final part, due to cooling between layers. To better predict this part weakness, this paper seeks to quantify how the toolpath affects the thermal history of a cross-section, thus impacting the formation of weld strength between printed layers. This is pertinent to in-situ embedding as different embedded geometries will require different cavity designs, which, in turn, will affect toolpath design. In-situ thermal measurements are experimentally collected with a thermocouple at the layer interface of structures with different cavity designs. The weld strength between layers is then obtained through tensile tests and theoretically evaluated using polymer weld theory. Results show more accurate predictions of load at failure with this method.

### 1. Introduction

The layer-by-layer nature of Additive Manufacturing (AM) provides an opportunity to embed sensors, actuators, circuits, and other functional components within a part, during the manufacturing process [1,2]. For in-situ embedding with the material extrusion process, first, a cavity is designed in the part and the printing process is paused once the cavity is printed. The foreign component is inserted into the cavity, and the print is resumed. This integrates the functionality of the inserted components into structures along with the offered flexibility in viable designs. This capability recently has been recognized for its application to the design and production of optimized electronics in aerospace industries and sophisticated “smart” objects [3–7]. The flexibility in manufacturing offered by AM allows cost effective manufacturing of customizable embedded electronics for applications where weight and volume is critical to overall performance. Various assembly-related processes and resource waste are eliminated with in-situ embedding, which makes AM a vital tool contributing towards the vision of Industry 4.0 to revolutionize manufacturing.

While in-situ embedding with AM shows potential for the future of manufacturing, its layer-by-layer process also presents with some limitations. AM structures are specifically weaker in the build direction [2,8]. Furthermore, cavities must be designed with orientations that allow foreign components to be completely submerged into the part to avoid any damage to the print head [9]. However, prior research has shown that the required process interruption for embedding process directly reduces the tensile strength of printed parts [10]. The introduced weakness at the paused layer, as well as further reduction of part strength due to the designed embedding cavity, raises concern over direct manufacturing of products via in-situ embedding with AM.

To address these weaknesses due to embedding, understanding how various factors in the process directly influence the part strength is important. One such factor in the material extrusion process is the thermal history at the interface of deposited material, that has been known to directly control the part strength [11,12]. This thermal history is subject to change with the material, ambient temperature, printing parameters like speed or layer height, and the material deposition toolpath [12–14]. Previous studies have almost exclusively focused on either the impact of these process parameters on the strength of the AM structures or the material's behavior under the processing temperature. To build this gap in design and theory of materials, this research focuses on investigating effects of different cavity designs for embedding on thermal history between the layers, especially due to different toolpath of material deposition. For this purpose, printed structures with different embedding cavity designs are studied with a computerized tomography (CT) scans, and the cross section area is categorized on the basis of the toolpath. Thermal measurements are obtained for each of these categories and polymer weld theory is utilized for prediction of strength. The predictions are then validated through uniaxial tensile tests.

## **2. Literature Review**

The following sub-sections summarize literature of relevance to the in-situ embedding process with material extrusion AM. The next section details the design for embedding considerations. Section 2.2 describes the link between toolpath and temperature of the layer interface. Section 2.3 details the polymer theory for predicting strength.

### *2.1 Design for in-situ embedding*

As with other manufacturing processes, a successful AM part with embedded components requires certain design considerations before manufacturing. To avoid damage to the print head or the embedded component, cavities must be designed so that the component is completely submerged and secured into the print [15–17]. Direct writing techniques to manufacture electronics also require process-based design planning such that the wire interconnects are accurately formed [18–21]. While these literatures focus on exploring applications and development of hybrid processes for embedding, few studies address the design for embedding considerations needed to retain the structural strength of the printed part [22].

Research suggests that careful design of cavities is essential for viable in-situ embedding. However, these cavities can also act as defects and directly affect the part's strength. Furthermore, the presence of cavities also influences the toolpath for material deposition. For example, in a material extrusion process, each layer starts by printing perimeters or shells. These shells define the boundary of the layer, according to the shape of that layer (See Figure 1). Research has shown that the presence of these shells is essential for the final quality of the part and directly influences the finish and strength of the structures [23–25]. The layers with the embedding cavities have additional perimeters defining the boundary of the cavity itself. Next, the empty spaces inside the perimeters are filled with the infill, for which users can typically select both density and pattern. A large body of literature exists that centers on optimizing the toolpath to minimize the time to print a layer [26–28]. Few address toolpath optimization based on structural strength [29]. However, for embedding, the strength between layers is of particular interest as the process is typically must be paused between the layers. This process interruption has been shown to directly

weaken the structure at the paused layer in prior research [10,22]. This strength is dictated by the thermal history of the interface.

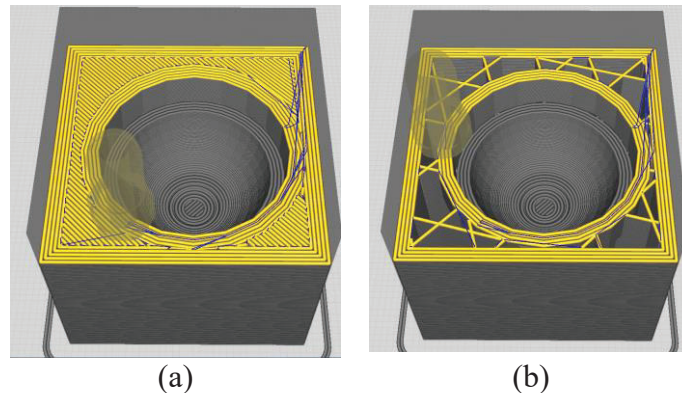


FIGURE 1. Shows the digital layer display in the Cura software, for a print layer. (a) Shows the toolpath for a 100% dense print with rectangular pattern infill. (b) Shows a toolpath for 20% dense infill for a triangular pattern infill.

## 2.2 Toolpath and thermal history

In order to increase the interfacial strength between layers for in-situ embedding AM, the thermal history, and thus the toolpath, must be considered. A typical desktop polymer material extrusion process uses polymer filament material that is fed in the nozzle, melted, and deposited layer by layer [30]. As the molten polymer is deposited in its viscous state, it cools and solidifies into roads of elliptical cross section due to the shear force on material by the nozzle [12–14]. This also leads to inbuilt air gaps between the road and the layers, which impact the overall strength of the structure [31–33]. The final strength of the part depends on the thermal history at the interface of the deposited and depositing roads; this thermal history defines the weld strength at the layer interfaces [12,14,34,35].

The thermal history at the layer interface depends on the toolpath, since the toolpath defines the location of molten material over time [11,14]. As discussed in Section 2.1, the toolpath varies in different regions and thus varies the thermal history at the layer interface. This results in differences in weld strength at each point of the embedding cross section [36,37]. A series of literature has indicated that all the print parameters that directly influences part strength can be attributed to the thermal history at the material interface [11,12]. To predict how this thermal history leads to weld formation in printed parts, it is necessary to understand the polymer's unique response to temperature quantified through its rheology [35].

## 2.3 Prediction of weld formation in polymer material

Thermal bonding or weld formation at the interface depends on material in processing and how cohesion occurs in that material. A polymer's behavior with temperature is unique because the long polymer chain molecules exhibit random motion at higher temperatures. This motion is known as reptation and causes polymer molecules to entangle with each other [38]. These entanglements result in cohesion at the interfaces. However, polymer molecule reptation is highly dependent on the time for which it stays at any elevated temperature. In isothermal states, the degree of cohesion can be directly measured with Ezekoye equation [34], using knowledge of the polymer's reptation time. Reptation time is the time taken by the polymer chain to completely

move out of its initial boundary at a given temperature [34]. The Ezekoye equation for estimating the weld strength at the interface is:

$$\frac{\sigma_{\text{weld}}}{\sigma_{\text{UTS}}} = \left( \frac{t}{\tau_{\text{rep}}} \right)^{\frac{1}{4}} \quad (1)$$

Here,  $\sigma_{\text{weld}}$  is the weld strength formed at an interface when it stays at a high temperature for time  $t$ ,  $\tau_{\text{rep}}$  is the reptation time for the polymer material at that temperature, and  $\sigma_{\text{UTS}}$  is the ultimate tensile strength of the bulk material. The interface between the polymer material will heal to 100% and exhibit the bulk-strength if it stays at a high temperature for the duration of reptation time for that temperature. Wool and O'Connor [38] used this equation to estimate the degree of healing in a polymer interface in isothermal conditions. Bartolai et al. [8] used equation 1 to develop a strength predicting “weld theory” for the non-isothermal case of material extrusion AM, which requires reptation time as a function of temperature. They demonstrated that by collecting thermal history at the road interfaces, and incorporating air gaps in the cross-sectional area measurements, the model was successful in predicting strength. The weld theory uses the above equation for non-isothermal interfaces by breaking the thermal history information into time steps, and integrating for each time step consecutively, with the following equation:

$$\sigma_{\text{weld}_f} = \sigma_{\text{UTS}} - (\sigma_{\text{UTS}} - \sigma_{\text{weld}_i}) \exp \left[ - \left( \frac{t_f - t_i}{\bar{\tau}_{\text{rep}}} \right) \right] \quad (2)$$

Where,  $\sigma_{\text{weld}_f}$  is the final weld strength at time  $t_f$ ,  $\sigma_{\text{weld}_i}$  is the initial weld strength at time  $t_i$ ,  $\sigma_{\text{UTS}}$  is the ultimate tensile strength of the polymer, and  $\bar{\tau}_{\text{rep}}$  is the average reptation time evaluated for the time step ( $t_f - t_i$ ). For each subsequent time step in the thermal history, the obtained  $\sigma_{\text{weld}_f}$  is used as the new  $\sigma_{\text{weld}_i}$ . Bartolai et al. demonstrated the applicability of equation 2 in predicting the weld strength along the X-Y direction of the build. However, for in-situ embedding, the process must be paused between the layers. Therefore, it is necessary to adapt the previous weld theory to predict the strength along the Z direction of the build.

### 3. Materials and Methods

The aim of this paper is to use polymer weld theory to predict weld strength between layers for printed specimens with different toolpath designs. This will enable an understanding of how the cavity design affects the strength of the structures. As discussed, the strength of welding between the layers is directly correlated with the thermal history at the interface [11,37]. Therefore, thermal history measurements of the layer interfaces were first obtained. CT scans of the printed specimens were then taken to obtain the actual contact area of the embedding layer's cross section. The cross sections were divided into zones of similar thermal history based on the type of toolpath (i.e., boundary, infill). To use the polymer weld theory for strength prediction, material rheology measurements were also made. Finally, to validate the strength predictions, experimental specimens were tensile tested until failure. The following sections discuss these methods in detail.

#### 3.1 Specimen design and preparation

To analyze the strength between layers, a series of tensile specimens were designed and printed upright, with their length along the Z direction of the build plate. However, ASTM standard tensile

specimens require smaller cross section areas than necessary to accommodate cavities for embedding. Therefore, a rectangular specimen of cross section 24 mm × 12 mm and length 96 mm was specially designed for the purpose of tensile tests. A series of control specimens were prepared without an embedding cavity; these then serve as the baseline for comparison. In order to make the results of this research broadly applicable, basic primitive geometries (e.g., cuboid, triangular prism, and cylinder) were chosen for the initial cavity designs. Each printed tensile specimen was designed with the cavity located at the geometric center of the specimen. Groups of samples with four different cuboid orientations (denoted as Cu1, Cu2, Cu3, and Cu4, as seen in Figures 2a, 2b, 2c, and 2d, respectively) were prepared. It is crucial to note that, each different orientation results in a different cavity cross-sectional area at the specimen's embedding plane. Additionally, a group of samples with an equilateral triangular prism cavity (denoted as Prism, Figure 2e) and a group with a cylindrical cavity (denoted as Cyl, Figure 2f) were prepared.

All build preparation and manufacturing parameters were kept consistent with a layer height of 0.2 mm and 100% infill density, prepared with Cura-lulzbot-3.2.27 software. The toolpath was automatically generated in the Cura software; this results in each specimen groups exhibiting a different toolpath due to differences in cavity cross-section. The natural PRO Series PLA (Polylactic acid) 3 mm filament by MatterHackers™ was used to print the specimen with a desktop material extrusion system (Lulzbot Taz 6). Specimens were printed one at a time, oriented with their length (96 mm) along the Z axis and their base centered on the build plate. An MTS 100 system with a 3000 lbf load cell was used to conduct uniaxial tensile tests until the specimens failed. A pull rate of 0.05 mm/sec was applied until failure using wedge action grips.

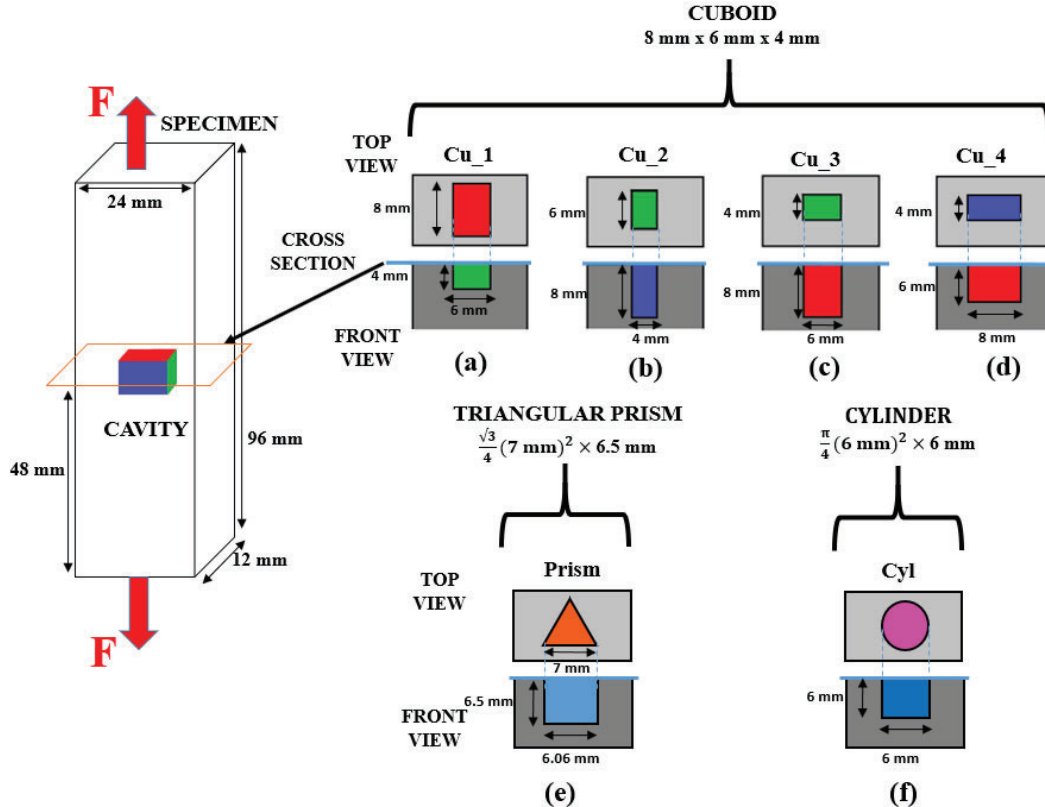


FIGURE 2. Specimen groups with different cavity designs.



### 3.2 Thermal history and cross section area measurements

As discussed before, different specimen toolpaths lead to a unique thermal history at each point of the cross section. Unfortunately, capturing this comprehensive thermal history experimentally is challenging due to obstruction from the motion of the printing nozzle. Therefore, to simplify measurement, the cross section of each specimen was divided into three zones: shell, infill, and infill boundary (see Figure 3). The shell zone occurs at the external perimeter of the cross section (shown in orange in Figure 3), while the infill zone is the central area of the cross-section filled with alternating roads of material (shown in green in Figure 3). Finally, the infill boundary zone (shown in blue in Figure 3) occurs where the infill meets the shells. In this zone, the tool changes direction, which causes it to decelerate, stop, and then accelerate. This results in a concentration of thermal energy as well as thicker material deposition [8].

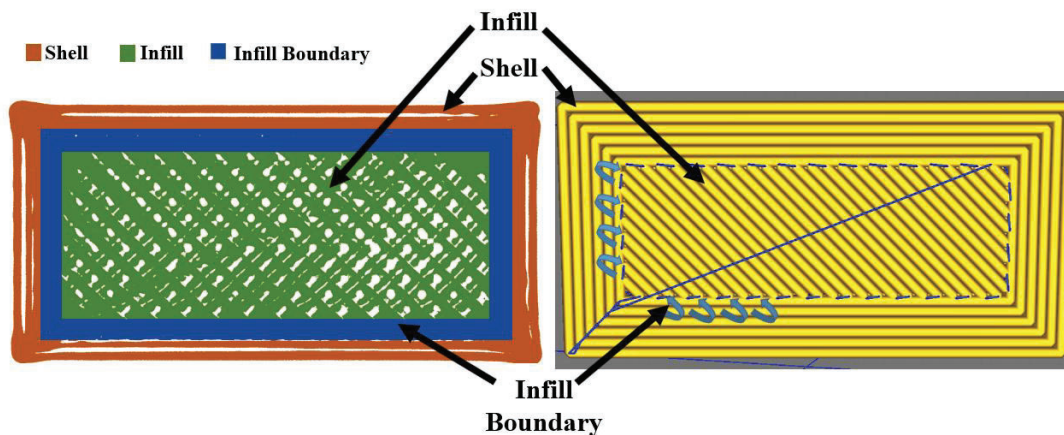


FIGURE 3. The shell, infill, and the infill boundary zones in the cross section of a control specimen. The air gaps are visible as white spaces between the deposited roads in the CT scanned slice of the cross section (left)

As shown in Figure 3, the deposition of polymer roads naturally results in air gaps present in each layer. As such, to obtain the actual cross-sectional area necessary for weld strength calculations, samples were CT scanned with a GE v|tome|x L300 multi-scale nano/micro CT system at a 16-micron resolution. The software program Image J was used for analysis of the obtained scans. The image slices were converted to binary, representing scanned point cloud data as black (0) or white (255) for analysis. The CT scanned slices were sectioned into shell, infill, and infill boundary zones and the area of each zone was calculated. Three slices were assessed for each group by counting the number of colored pixels in each zone using Image J. For the infill zone, this calculation includes overhanging roads that are not in contact between the layers due to the changing infill orientation in each layer. To compensate for overestimation of infill contact area, the computed cross-section area of each infill zone was reduced by half for future calculations.

To experimentally determine the thermal history of each of the three toolpath zones, a thermocouple was used to capture the temperature-time data for each zone during printing. A type J thermocouple (KK-J-245) by OMEGA Engineering was used to obtain the thermal history at the interface (see Figure 4b and 4c) through a DI-245 by DATAQ instruments data acquisition system. Holes were designed in the control specimen to allow the thermocouple wires to be embedded.

The print was paused once the holes were printed, then the two thermocouple wires were inserted and brought in contact at the paused layer. Once the build is resumed, the thermocouple should capture the thermal history at the interface between the paused and the resumed layer (Figure 4d). The thermal histories for the three zones were obtained by carefully positioning the thermocouple contact point in these zones for a control specimen. Two measurements for each of the zones were repeated for consistency in measurements.

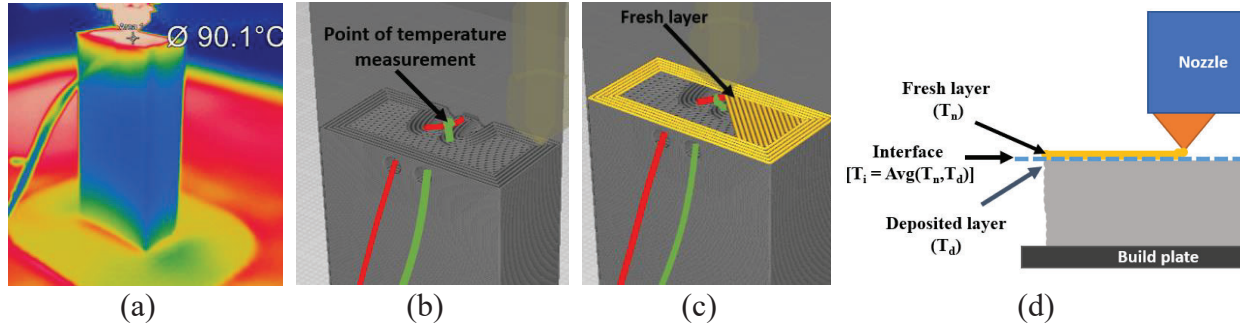


FIGURE 4. (a) Snapshot from the IR camera while recording the thermal history. (b) Embedded thermocouple wires in red and green, through the designed cavity, connected at the exposed paused layer. (c) Shows the location of thermocouple at the interface of deposited and resumed layer. (d) Shows the representation of the print, and the layer interface location with respect to the deposited and the fresh layer.

When pausing the print to place the thermocouple wires in the specimen, the topmost layer will naturally cool down more than would be observed in continuous print. This may skew calculation of the average thermal history between layers. Because of this, an IR camera (Optris Pi 450, by Optris GmbH, with Optris Pi Connect thermal imaging software) was also used to collect the temperature-time data at the topmost visible layer of a continuous printing process (see Figure 4a). The temperature data from the IR camera shows that, in a continuous print, the previously deposited layer has already cooled to  $\sim 60$  °C at the moment that a fresh layer is deposited. However, the necessary pause to embed the thermocouple causes the previously deposited layer to cool down to  $\sim 35$  °C at the moment a new layer is deposited (a discrepancy of  $\sim 25$  °C). Assuming that the temperature at the interface is an average of the temperature of the paused layer and the freshly deposited layer (Figure 4d), the interface temperature history for a continuous print can be estimated by adding 12.5 °C to the interface temperature obtained from the thermocouple.

### 3.3 Polymer material rheology for weld strength

To calculate the weld strength from Equation 2,  $\bar{\tau}_{rep}$  of the material as a function of temperature is required. However, as discussed in Section 2.3, the strength prediction from polymer weld theory is only valid for temperatures at which the polymer molecules reptate. Previously, Bartolai et. al. used the temperature history only above the  $T_g$  value for both Polycarbonate (PC) and Acrylonitrile butadiene styrene (ABS); this temperature allows the weld forming polymer molecule movements to occur [8,14]. While both PC and ABS materials are amorphous in nature, exhibiting a clear  $T_g$  region, the PLA material used in this research is semi-crystalline. The partial crystalline arrangement of its molecules inhibits their movement until its melting temperature is reached [39], which suggests that PLA molecules will only diffuse and weld when the polymer is at its molten state [40,41]. Therefore, to predict the weld strength

formation at the layer interface, only the thermal history for the polymer is at its molten state is required. To obtain the melting temperature for PLA, Digital Scanning Calorimetry (DSC) experiments were performed for a heat-cool-heat cycle, where the material was heated from 25 °C to 170 °C at a rate of 10°C per minute. The melting peak occurred at approximately 148.6 °C for both heat cycles, with the end of the peak occurring at 150 °C. Since the reptation of molecules that causes adhesion occurs only in PLA's molten state, only the temperature history of the fresh layer above 150°C is of interest for predicting the strength. Therefore, only the temperature values above 150 °C in the thermal history of the fresh layer was considered in this research. Accordingly, the interface temperature values (which is assumed to be an average of the temperature values of the fresh layer and the deposited layer), resulting in predicted fresh layer temperature above or equal to 150 °C were considered for prediction.

After identifying the temperature region of interest for PLA, material rheology measurements were made. Hot pressed PLA disks were prepared and storage and loss modulus were obtained using a strain-controlled ARES rotational rheometer. Measurements were performed at angular frequency range of 0.5 rad/s to 100 rad/s, at strain rate of 1% for every 10 °C from 160 °C to 200 °C. For viscoelastic materials, these isothermal sweeps do not change in shape but only shift along the time axis with temperature (see Figure 5a), which makes it possible to obtain a master curve at a desired reference temperature ( $T_{ref}$ , see Figure 5b). This phenomenon, known as the time-temperature superposition (TTS) principle, uses a temperature-dependent translation factor,  $a_T$  to perform a shift operation on the master curve. This enabled calculation of the isothermal modulus properties for any other temperature. The function of  $a_T$  is obtained through the Williams-Landel-Ferry (WLF) model [42], shown in Equation 3:

$$a_T(T) = \exp\left(\frac{-C_1(T-T_{ref})}{C_2+(T-T_{ref})}\right) = \frac{\tau_{rep}(T)}{\tau_{rep}(T_{ref})} \quad (3)$$

Where  $a_T$  is the temperature dependent translation factor,  $T$  is the temperature of interest,  $T_{ref}$  is the reference temperature, which is used for TTS,  $C_1$  &  $C_2$  are WLF constants that can be obtained by fitting the experimental values for that reference temperature. A reference temperature of 180 °C was used with corresponding WLF constant for further calculations. The reptation time ( $\tau_{rep}$ ) for PLA at 180 °C is simply the inverse of the frequency at which storage modulus equals loss modulus at that temperature. The  $\tau_{rep}(180\text{ °C})$  was experimentally evaluated as 1/94.2684 rad/s or 1/15 seconds. With this obtained reptation time, equations 2 and 3 can be used to calculate weld strength for a given thermal history.



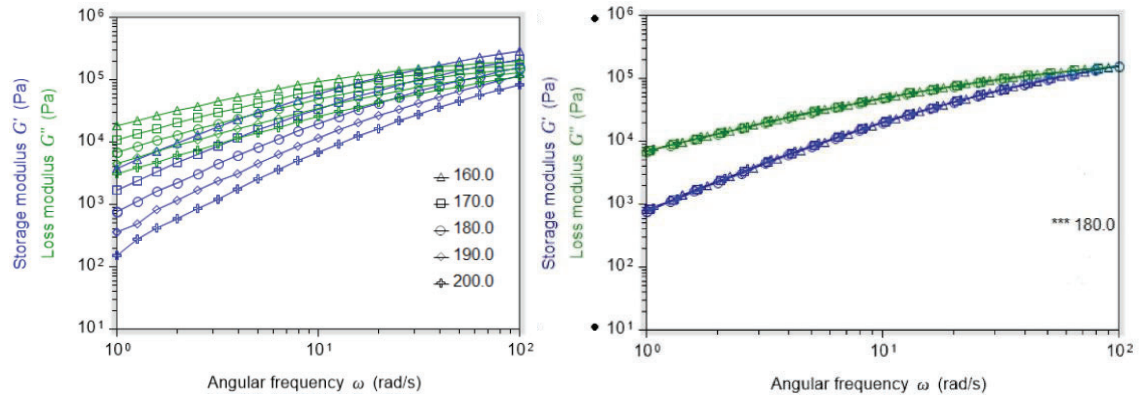


FIGURE 5. (a) Isothermal time-temperature superposition (TTS) of storage modulus and loss modulus for PLA, and (b) TTS master curve at reference temperature 180 °C.

#### 4. Results and Analysis

This section uses the methods from Section 3 to predict the tensile load at failure for specimens with different in-situ embedding cavities. This prediction leverages both contact area and thermal history at layer interfaces. To validate the accuracy of the prediction, experimental tensile tests are also conducted.

##### 4.1 Impact of cavity design on thermal history at the interface

The cross-sectional area was measured through the CT scanned images of the interfaces, as detailed in Section 3.2. The total cross-sectional area for each specimen lies in the range of 164 to 185 mm<sup>2</sup>, but the cross-sectional area distribution between the zone types change notably depending on cavity geometry. CT data, summarized in Table 1, shows that, since the presence of a cavity introduces more perimeters, more cross-sectional area becomes dedicated to the shell zone (see Figure 6.).

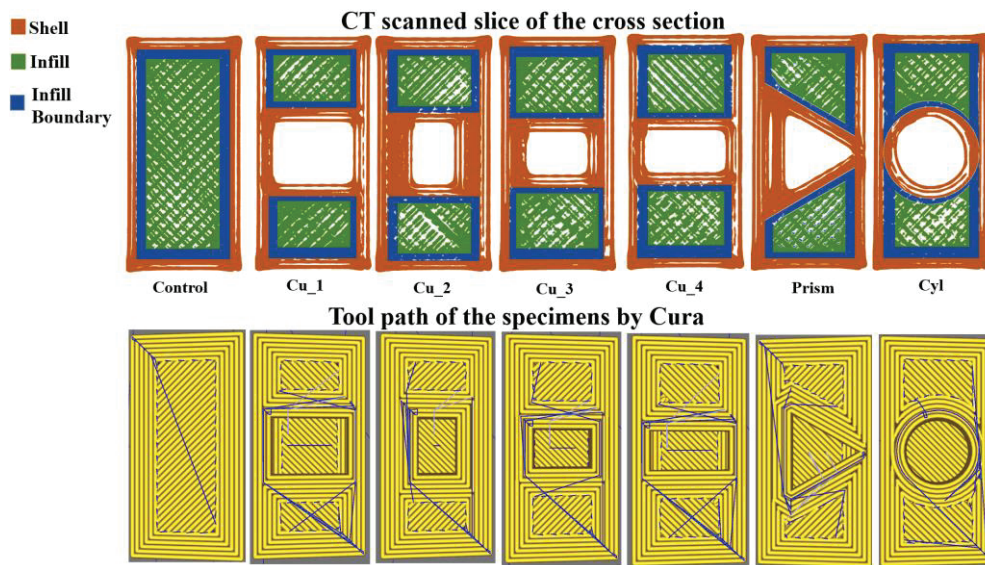


FIGURE 6. CT scanned slice and digital slice of the specimen.

TABLE 1. Cross section area distribution within the different samples.

Groups	Shell		Infill		Infill Boundary		Total c/s area (mm <sup>2</sup> )
	Area (mm <sup>2</sup> )	% of total	Area (mm <sup>2</sup> )	% of total	Area (mm <sup>2</sup> )	% of total	
Control	70.9	39%	61.3	33%	50.8	28%	183.0
Cu1	83.1	51%	32.7	20%	48.2	29%	164.0
Cu2	83.5	46%	40.8	23%	55.8	31%	180.0
Cu3	75.8	41%	36.0	19%	73.7	40%	185.5
Cu4	79.9	48%	35.6	21%	51.0	31%	166.5
Prism	102.3	55%	31.3	17%	51.3	28%	184.9
Cyl	93.4	51%	30.0	16%	58.3	32%	181.7

For each of the three zones, the thermal history was obtained by carefully positioning the thermocouple wires in the control specimen's cross section, as discussed in Section 3.2. The resultant temperature history for each zone is shown in Figure 7. In the plot, abrupt jumps in temperature denote the deposition of molten material in close proximity to the thermocouple. The smooth curves that follow after each peak quantify the rate of cooling at the interface after material deposition. These results show that each zone exhibits a distinctly different thermal history. The next section validates the prediction of weld strength with these thermal histories and the cross sectional area of each zone obtained for the different cavity geometries.

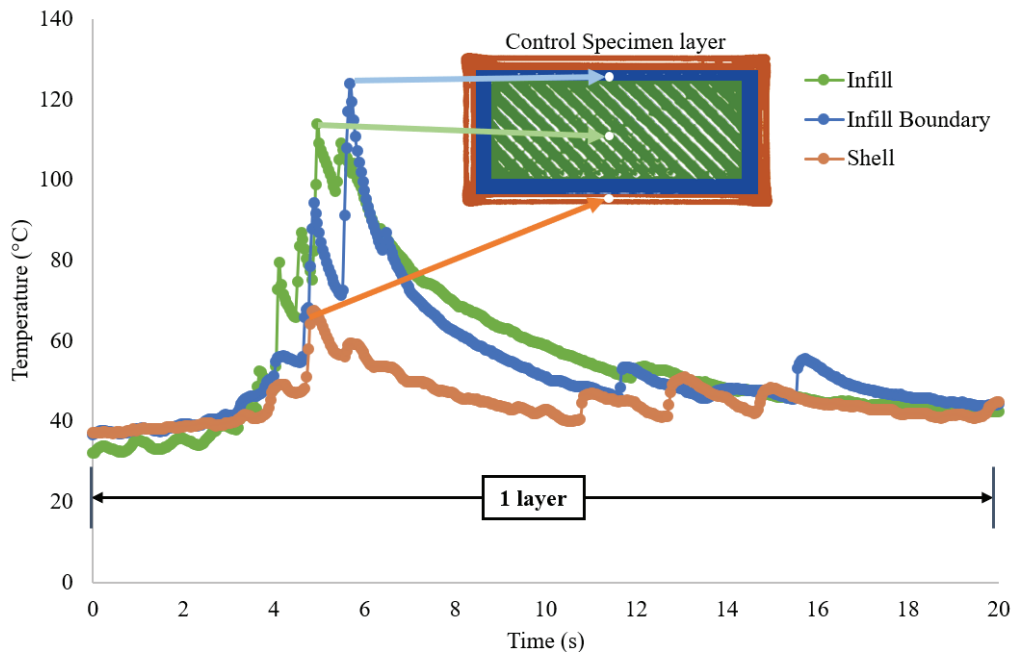


FIGURE 7. Thermal history as obtained by the thermocouple for each zone for one layer of material deposition with the location of measurement in the control specimen cross section.

#### 4.2 Validation failure load predictions using weld theory and rule of mixtures

As discussed, the different thermal history in each of the three cross-sectional zones leads to different weld strength formation for each of them. Therefore, to simplify prediction, these AM structures can be treated as composites made from sections with different strength values. Under

this assumption, the rule of mixtures can be used to calculate the total load in the cross section by the using the following equation:

$$F_{predicted} = \sigma_s A_s + \sigma_i A_i + \sigma_{ib} A_{ib} \quad (4)$$

Where  $F_{predicted}$  is the predicted tensile load at failure, and  $\sigma_s, \sigma_i, \sigma_{ib}$  are the predicted weld strength for the shell, infill, and infill boundary zones, respectively. Similarly,  $A_s, A_i,$  and  $A_{ib}$  are the actual cross-sectional areas in each of the three zones. The ultimate tensile strength ( $\sigma_{UTS}$ ) for PLA was taken as 50 MPa [43].

With the known function of  $\tau_{rep}(T)$  from Equation 3, the  $\bar{\tau}_{rep}$  for each time step from the recorded thermal history was obtained and substituted in Equation 2. The time step ( $t_f - t_i$ ) was taken as 0.04 seconds, which is equal to the resolution of the data acquisition system for the thermocouple. Subsequent calculations for each time step where the freshly deposited layer was above the melting temperature (150 °C) gave the predicted final weld strength. Through Equations 2 and 3, the weld strength of the shell, infill, and the infill boundary zones were obtained as **27 MPa, 45.3 MPa, and 39.2 MPa**, respectively. The failure load for specimens with different embedding cavity geometries were then predicted using Equation 4.

The results of tensile tests of different embedding cavity specimens, along with their predicted strength values derived from polymer weld theory are shown in Figure 8. For comparison, the figure also shows the predicted load at failure if the cross section were not divided into zones, and only the total area was used by assuming one thermal history throughout the cross section.

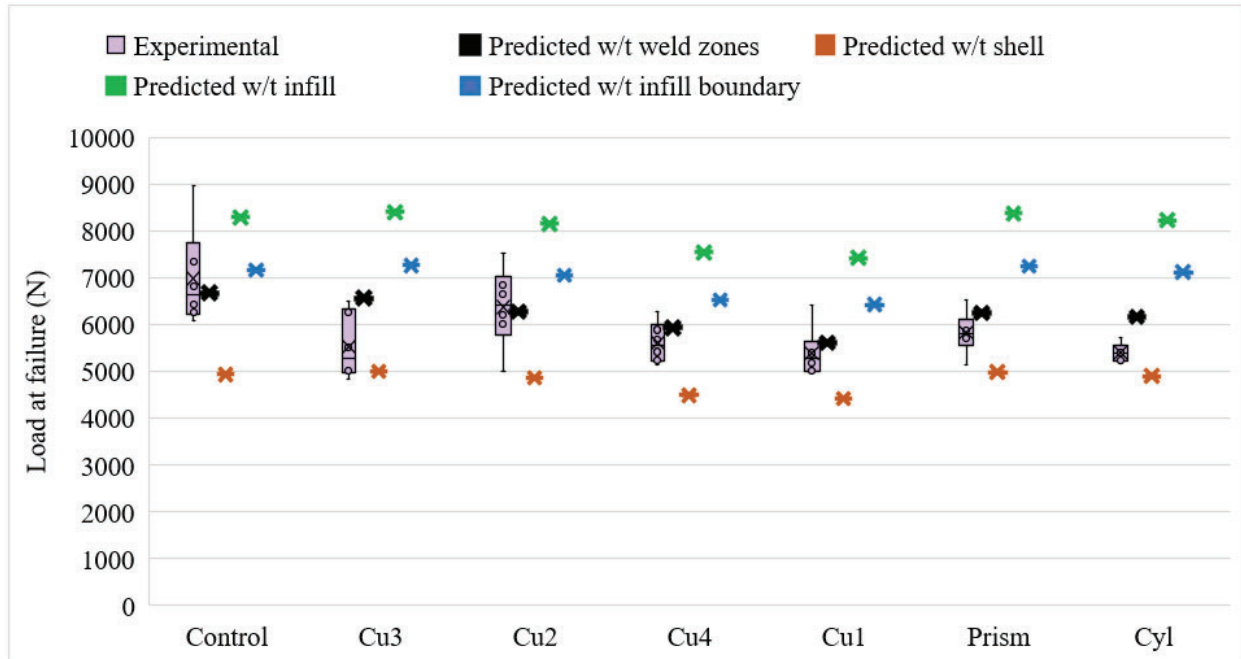


FIGURE 8. Experimentally obtained and predicted tensile load at failure for all the groups of specimens.

TABLE.2. Summary of the experimental and predicted loads at failure for the groups with errors.

Groups	Predicted load distribution in the cross section (N)			Tensile load at failure		
	Shell	Infill	Infill Boundary	Predicted (N)	Experimental Avg (N)	% error
<b>Control</b>	1915.0	2776.9	1991.6	6683.5	6991.6	5%
<b>Cu3</b>	2047.6	1632.2	2889.1	6568.9	5530.9	16%
<b>Cu2</b>	2253.8	1848.4	2187.8	6290.0	6384.3	1%
<b>Cu4</b>	2158.4	1613.6	1999.5	5771.5	5614.1	5%
<b>Cu1</b>	2243.3	1480.5	1890.8	5614.7	5400.5	4%
<b>Prism</b>	2761.9	1419.0	2012.5	6193.4	5831.8	7%
<b>Cyl</b>	2521.6	1358.4	2285.8	6165.8	5404.0	12%

Cyl and Cu3 groups show high error in strength prediction by considering the three weld zones. The experimental load at failure were lower than predicted for these two groups. Qualitative observations show that under extrusions in the infill zone were the reason for low strength value. Furthermore, 80% of the tensile failures for the cavity specimens occurred at the layer where the cavity started or ended printing. Stress concentrations due to the abrupt start of the cavity could explain this location of failure. The other 20% of the time, the failure occurred at layers with the cavity. With the added process interruption required for embedding, this location of failure is expected to be the paused layer due [10,22].

As is evident from the Figure 6 and Table 2, the proposed method of dividing the cross section into weld zones and leveraging them to predict the load at failure through the rule of mixtures more accurately predicts the load at failure than assuming a constant thermal history throughout a printed layer. This method results in prediction error as low as 1%, depending on the geometry of the embedding cavity. By comparison, approximating the cross section as a bulk with only one thermal history either under- or over-predicts the load at failure. Establishing this understanding is a crucial step toward enabling engineers to account for cavity geometry and toolpath design in their estimation of part strength for multi-functional embedded AM parts.

## 5. Conclusion and Future Work

The research presented in this paper proposes a method to predict the strength of parts with different cavity design for embedding applications with material extrusion AM. The thermal history of printed layers is used in conjunction with PLA's rheology behavior to predict the strength between the layer interfaces using the weld theory by Bartolai et. al [8]. Interfaces were considered as composites made of zones with different thermal histories. The experimental results confirm that this method of considering thermal history in a layer results in more accurate predictions of failure load when compared with assuming a constant thermal history across the layer. This demonstrates the importance of toolpath design when incorporating cavities to support in-situ embedding in AM.

This research demonstrates that the thermal history at the layer interface as a result of the toolpath and material distribution has a considerable impact on printed part strength. However, the methods presented approximated the thermal history for each cross-sectional zone as one, due to limitations in the thermal data collection techniques. Additionally, variations in the speed of material deposition due to changes in toolpath direction were ignored. Because of the high sensitivity of the thermal histories to the toolpath, these effects should be considered to improve

prediction accuracy. This requires development of a computational tool to more precisely consider toolpath design and capture thermal history at each point in a layer. The thermal histories for each point can then be used to improve the accuracy of weld strength prediction between the layers.

## 6. References

- [1] Kumar, V., Rajagopalan, S., Cutkosky, M. R., and Dutta, D., 1998, "Representation and Processing of Heterogeneous Objects for Solid Freeform Fabrication," *Geom. Model. Work.*, pp. 1–21.
- [2] Meisel, N. A., Elliott, A. M., and Williams, C. B., 2015, "A Procedure for Creating Actuated Joints via Embedding Shape Memory Alloys in PolyJet 3D Printing," *J. Intell. Mater. Syst. Struct.*, **26**(12), pp. 1498–1512.
- [3] Leu, M., Xiao, H., and Dong, J., 2015, "Additive Manufacturing of Smart Parts with Embedded Sensors for In-Situ Monitoring in Advanced Energy Systems Investigators : Program Manager :"
- [4] Geller, S., and Gude, M., 2015, "Process-Integrated Manufacturing and Embedding of Novel Piezoelectric Sensor Modules into Glass Fibre-Reinforced Polyurethane Composite Structures," *Mater. Sci. Forum*, **825–826**, pp. 563–570.
- [5] Maier, R. R. J., MacPherson, W. N., Barton, J. S., Carne, M., Swan, M., Sharma, J. N., Futter, S. K., Knox, D. A., Jones, B. J. S., and McCulloch, S., 2013, "Embedded Fiber Optic Sensors within Additive Layer Manufactured Components," *IEEE Sens. J.*, **13**(3), pp. 969–979.
- [6] Willis, K. D. D., Brockmeyer, E., Hudson, S. E., and Poupyrev, I., 2012, "Printed Optics: 3D Printing of Embedded Optical Elements for Interactive Devices."
- [7] Kwas, A., MacDonald, E., Kief, C. J., Wicker, R., Soto, C., Bañuelos, L., Aarestad, J., Zufelt, B., Stegeman, J. D., and Tolbert, C., 2014, "Printing Multi-Functionality: Additive Manufacturing for CubeSats," *AIAA Sp. 2014 Conf. Expo.*, (August), pp. 1–9.
- [8] Bartolai, J., Simpson, T. W., and Xie, R., 2018, "Predicting Strength of Additively Manufactured Thermoplastic Polymer Parts Produced Using Material Extrusion," *Rapid Prototyp. J.*, **24**(2), pp. 321–332.
- [9] Manoj Malvia, Swapnil Sinha, N. A. M., 2019, "Digital Design Automation to Support in-Situ Embedding of Functional Components in Additive Manufacturing," *Proceedings of the ASME International Design Engineering Technical Conferences & Computer's and Information in Engineering Conference*, Anaheim, CA, [IN PRINT].
- [10] Sinha, S., and Meisel, N. A., 2018, "Influence of Process Interruption on Mechanical Properties of Material Extrusion Parts," *Rapid Prototyp. J.*, p. RPJ-05-2017-0091.
- [11] Seppala, J. E., Hoon Han, S., Hillgartner, K. E., Davis, C. S., and Migler, K. B., 2017, "Weld Formation during Material Extrusion Additive Manufacturing," *Soft Matter*, **13**, pp. 6761–6769.
- [12] Davis, C. S., Hillgartner, K. E., Han, S. H., and Seppala, J. E., 2017, "Mechanical Strength of Welding Zones Produced by Polymer Extrusion Additive Manufacturing," *Addit. Manuf.*, **16**, pp. 162–166.
- [13] Gurralla, P. K., and Regalla, S. P., 2014, "Part Strength Evolution with Bonding between Filaments in Fused Deposition Modelling: This Paper Studies How Coalescence of Filaments Contributes to the Strength of Final FDM Part," *Virtual Phys. Prototyp.*, **9**(3), pp. 141–149.
- [14] Bartolai, J., 2018, "Predicting and Improving Mechanical Strength of Thermoplastic



- Polymer Parts Produced by Material Extrusion Additive Manufacturing,” The Pennsylvania State University.
- [15] Kataria, A., and Rosen, D. W., 2001, “Building around Inserts: Methods for Fabricating Complex Devices in Stereolithography,” *Rapid Prototyp. J.*, **7**(5), pp. 253–261.
  - [16] Meisel, N. A., Elliott, A. M., and Williams, C. B., 2015, “A Procedure for Creating Actuated Joints via Embedding Shape Memory Alloys in PolyJet 3D Printing,” *J. Intell. Mater. Syst. Struct.*, **26**(12), pp. 1498–1512.
  - [17] Aguilera, E., Ramos, J., Espalin, D., Cedillos, F., Muse, D., Wicker, R., and MacDonald, E., 2013, “3D Printing of Electro Mechanical Systems,” *Proceedings of the 24th Solid Freeform Fabrication Symposium (SFF)*, Univ. of Texas at Austin, Austin, Texas, pp. 950–961.
  - [18] Kadara, R. O., Jenkinson, N., Li, B., Church, K. H., and Banks, C. E., 2008, “Manufacturing Electrochemical Platforms: Direct-Write Dispensing versus Screen Printing,” *Electrochem. commun.*, **10**(10), pp. 1517–1519.
  - [19] Perez, K. B., and Williams, C. B., 2013, “Combining Additive Manufacturing and Direct Write for Integrated Electronics – A Review,” *Int. Solid Free. Fabr. Symp. Proc.*, pp. 962–979.
  - [20] Lewis, J. A., and Gratson, G. M., 2004, “Direct Writing in Three Dimensions,” *Mater. Today*, **7**(7), pp. 32–39.
  - [21] Espalin, D., Muse, D. W., MacDonald, E., and Wicker, R. B., 2014, “3D Printing Multifunctionality: Structures with Electronics,” *Int. J. Adv. Manuf. Technol.*, **72**(5–8), pp. 963–978.
  - [22] Sinha, S., and Meisel, N. A., 2018, “Quantifying the Effect of Embedded Component Orientation on Flexural Properties in Additively Manufactured Structures,” *Solid Freeform Fabrication 2018: Proceedings of the 29th Annual International*, Austin, Texas, pp. 1511–1525.
  - [23] Jennifer, E., and Medeiros, D., 2017, “Behaviour of Infill Building Strategies for Fused Deposition Modelling Objects,” pp. 984–991.
  - [24] 2016, “Shells Matter More than Meets the Eye,” 3D Matter [Online]. Available: <https://my3dmatter.com/shells-matter-more-than-meets-the-eye/>.
  - [25] Rodríguez-Panes, A., Claver, J., and Camacho, A. M., 2018, “The Influence of Manufacturing Parameters on the Mechanical Behaviour of PLA and ABS Pieces Manufactured by FDM: A Comparative Analysis,” *Materials (Basel)*, **11**(8).
  - [26] Jin, G. Q., Li, W. D., Tsai, C. F., and Wang, L., 2011, “Adaptive Tool-Path Generation of Rapid Prototyping for Complex Product Models,” *J. Manuf. Syst.*, **30**(3), pp. 154–164.
  - [27] Wah, P. K., Murty, K. G., Joneja, A., and Chiu, L. C., 2002, “Tool Path Optimization in Layered Manufacturing,” *IIE Trans. (Institute Ind. Eng.)*, **34**(4), pp. 335–347.
  - [28] Lensgraf, S., and Mettu, R. R., 2016, “Beyond Layers: A 3D-Aware Toolpath Algorithm for Fused Filament Fabrication,” *Proc. - IEEE Int. Conf. Robot. Autom.*, **2016–June**, pp. 3625–3631.
  - [29] Roschli, A., Messing, A., Borish, M., Post, B. K., and Love, L. J., 2017, “Ornl Slicer 2: A Novel Approach for Additive Manufacturing Tool Path Planning,” pp. 896–902.
  - [30] Rosen, D. W., 2007, “Design for Additive Manufacturing: A Method to Explore Unexplored Regions of the Design Space,” *Eighteenth Annual Solid Freeform Fabrication Symposium*, Austin, Texas, pp. 402–415.
  - [31] Rayegani, F., and Onwubolu, G. C., 2014, “Fused Deposition Modelling (Fdm) Process

- Parameter Prediction and Optimization Using Group Method for Data Handling (Gmdh) and Differential Evolution (de),” *Int. J. Adv. Manuf. Technol.*, **73**(1–4), pp. 509–519.
- [32] Sood, A. K., Ohdar, R. K., and Mahapatra, S. S., 2010, “Parametric Appraisal of Mechanical Property of Fused Deposition Modelling Processed Parts,” *Mater. Des.*, **31**(1), pp. 287–295.
  - [33] Ahn, S.-H., Montero, M., Odell, D., Roundy, S., and Wright, P. K., 2002, “Anisotropic Material Properties of Fused Deposition Modeling ABS,” *Rapid Prototyp. J.*, **8**(4), pp. 248–257.
  - [34] Ezekoye, A., 1998, “Polymer Weld Strength Predictions Using a Thermal and Polymer Chain Diffusion Analysis,” *Polym. Eng. Sci.*, (6), p. 976.
  - [35] McIlroy, C., and Olmsted, P. D., 2017, “Disentanglement Effects on Welding Behaviour of Polymer Melts during the Fused-Filament-Fabrication Method for Additive Manufacturing,” *Polymer (Guildf.)*, **123**, pp. 376–391.
  - [36] Ravi, A. K., Deshpande, A., and Hsu, K. H., 2016, “An in-Process Laser Localized Pre-Deposition Heating Approach to Inter-Layer Bond Strengthening in Extrusion Based Polymer Additive Manufacturing,” *J. Manuf. Process.*, **24**, pp. 179–185.
  - [37] Deshpande, A., Ravi, A., Kusel, S., Churchwell, R., and Hsu, K., 2018, “Interlayer Thermal History Modification for Interface Strength in Fused Filament Fabricated Parts,” *Prog. Addit. Manuf.*, **0**(0), p. 0.
  - [38] Wool, R. P., and O’Connor, K. M., 1982, “Time Dependence of Crack Healing,” *J. Polym. Sci. Polym. Lett. Ed.*, **20**(1), pp. 7–16.
  - [39] Boyd, R. H., 1985, “Relaxation Processes in Crystalline Polymers: Molecular Interpretation - a Review,” *Polymer (Guildf.)*, **26**(8), pp. 1123–1133.
  - [40] Yang, C., Tian, X., Li, D., Cao, Y., Zhao, F., and Shi, C., 2017, “Influence of Thermal Processing Conditions in 3D Printing on the Crystallinity and Mechanical Properties of PEEK Material,” *J. Mater. Process. Technol.*, **248**(January), pp. 1–7.
  - [41] Kuznetsov, V. E., Solonin, A. N., Urzhumtsev, O. D., Schilling, R., and Tavitov, A. G., 2018, “Strength of PLA Components Fabricated with Fused Deposition Technology Using a Desktop 3D Printer as a Function of Geometrical Parameters of the Process,” *Polymers (Basel)*, **10**(3).
  - [42] Williams, M. L., Landel, R. F., and Ferry, J. D., 1955, “The Temperature Dependence of Relaxation Mechanisms in Amorphous Polymers and Other Glass-Forming Liquids,” *J. Am. Chem. Soc.*, **77**(14), pp. 3701–3707.
  - [43] Farah, S., Anderson, D. G., and Langer, R., 2016, “Physical and Mechanical Properties of PLA, and Their Functions in Widespread Applications — A Comprehensive Review,” *Adv. Drug Deliv. Rev.*, **107**, pp. 367–392.